Electronic Supplementary Information: Tunable 2D Binary Colloidal Alloys for Soft Nanotemplating

Miguel Ángel Fernández-Rodríguez,[a,†] Roey Elnathan,[b,†] Ran Ditcovski,[c] Fabio Grillo,[a] Gaurasundar Marc Conley,[d] Flavia Timpu,[e] Astrid Rauh,[f] Karen Geisel,[g] Tal Ellenbogen,[c] Rachel Grange,[e] Frank Scheffold,[d] Matthias Karg,[f] Walter Richtering,[g] Nicolas H. Voelcker,[b,h] and Lucio Isa[a]*

Materials

The small and gold-core PNIPAM microgels synthesis is described in previous works [1,2]. The big microgels were synthesized following a standard protocol with NIPAM (Acros Organics, Sigma-Aldrich, 99%) as monomer, N,N-methylenebis(acrylamide) (Sigma-Aldrich, 99%) as crosslinker, 2,2-Azobis(2-methyl propionamidine)dihydrochloride (Sigma-Aldrich, 97%) as initiator and N-(3-aminopropyl)methacrylamide hydrochloride (Polysciences, Sigma-Aldrich) as co-monomer [3]. The latter allowed incorporating free amine groups into the microgels to be used as conjugation points for NHS ester-fluorescent Alexa dyes (488 nm Alexa Fluor Dye, Thermo Fisher Scientific). Microgels were dispersed at 1 wt% in 4:1 water:isopropanol mixtures previous to their deposition at MilliQ water/hexane (Sigma-Aldrich, 99%) interfaces. The substrates for deposition were cut from silicon wafers with a (100) orientation (Siltronix, p-type (boron-doped), 3 to $6\,\Omega cm$), in $1x2\,cm^2$ or $2x2\,cm^2$ pieces with a diamond pen. They were cleaned with subsequent ultrasonications of 15 min-each: in toluene (Fluka Analytical, 99.7%), isopropanol (Fisher Chemical, 99.97%), Milli-Q water and dried with N_2 gas.

Methods

Deposition methods

The microgels dispersed in 4:1 water:isopropanol mixtures were directly injected at the MilliQ water/hexane interface in a KSV5000 Langmuir Teflon-trough setup using a precision micro-syringe (Hamilton). The substrate previously immersed in the water subphase was lifted at speeds below 0.5 mm/min while the desired gradient or constant interfacial pressure was achieved by compressing with the Langmuir trough Delrin barriers. The different deposition parameters for the systems reported in the main paper are summarized in Table S1.

Characterization methods

The size and electrophoretic mobility of the microgels was measured in MilliQ water and as a function of pH, respectively, by dynamic light scattering (DLS, Zetasizer, Malvern UK). The pH was adjusted by drop-wise addition of 0.1 M HCl and 0.1 M NaOH. The deposited 2D binary colloidal alloys on silicon substrates were systematically characterized with an AFM in tapping mode (Bruker Icon Dimension, with Olympus cantilevers of 300 kHz resonance frequency and 26 N/m spring constant, 14 nm tip diameter, 0 and 35°of front and back tip angle, symmetric cone of <9°half-angle). The big microgels re-swelled in water were characterized with PeakForce Quantitative Nanoscale Mechanical mode (with a Scanasyst-Fluid+ cantilever, 150 kHz resonance frequency and 0.7 N/m spring constant). Then, the images were further analyzed using a custom-written Matlab particle-tracking software built around the particle-tracking code by Crocker and Grier [4], separating the analysis of the big and

[a] *Laboratory for Interfaces, Soft matter and Assembly, Department of Materials, ETH Zurich, 8093 Zurich, Switzerland; E-mail: lucio.isa@mat.ethz.ch*
[b] *Drug Delivery, Disposition and Dynamics, Monash Institute of Pharmaceutical Sciences Monash University, 381 Royal Parade, Parkville, Victoria, 3052, Australia.*
[c] *Department of Physical Electronics, School of Electrical Engineering, Tel Aviv University, Tel Aviv-Yafo, Israel.*
[d] *Department of Physics, University of Fribourg, CH-1700 Fribourg, Switzerland*
[e] *Institute for Quantum Electronics, Department of Physics, ETH Zurich, 8093 Zurich, Switzerland*
[f] *Physical Chemistry I, Heinrich-Heine-University Duesseldorf, 40204 Duesseldorf, Germany*
[g] *Physical Chemistry II, RWTH Aachen University, 52062 Aachen, Germany*
[h] *Melbourne Centre for Nanofabrication, Victorian Node of the Australian National Fabrication Facility, 151 Wellington Road, Clayton, Victoria, 3168, Australia*
INM-Leibniz Institute for New Materials, Campus D2 2, Saarbrücken, 66123, Germany
[†] M.A.F.R and R.E. contributed equally to this work.

Table S1. Deposition parameters for the systems reported in the main manuscript. Surface pressure during the first deposition of big microgels, subsequent O_2 plasma etching, and surface pressure of small microgels during the second deposition.

Figure	Π_{big} (mN/m)	O_2 plasma etching (s)	Π_{small} (mN/m)
Fig. 1c left	Fixed at 4	-	Fixed at 5
Fig. 1c right	Fixed at 2	20	Fixed at 2
Fig. 2a	Fixed at 2	-	3 to 22
Fig. 3a	Fixed at 1	-	Fixed at 6.5
Fig. 3b	Fixed at 1	-	Fixed at 6.5
Fig. 3c	Fixed at 2	-	1 to 19
Fig. 3f	Fixed at 1	-	2 (from a 2 to 21 gold-core gradient)

small particles by size of the detected features.

NW fabrication methods

After microgel deposition, the substrates were subjected to O_2 plasma to reduce the diameter of the big and small microgels. The deposited binary arrays were then swollen with AZ1518 (Clariant GmbH, Germany) photoresist. After 30 min exposure to the photoresist, the excess is removed with acetone as described in previous works[5,6]. In this step, the photoresist helps to increase the height and density of the microgels, which is required to provide enough material contrast to act as masks for wet etching. Next, a 10 nm-thick gold layer was deposited on the substrate with a sputter coater (CCU-010, safematic GmbH) at 30 mA and $3{\cdot}10^{-2}$ mbar. Metal-assisted chemical etching (MACE) was carried out in Teflon beakers, where the etching solution was composed of 6 mL of MilliQ water, 6 mL of ethanol (Fluka Analytical, 99.8%), 4 mL of hydrogen peroxide (Merck, 30%) and 4 mL of HF (Sigma Aldrich, 48%). Without the swelling step, the microgels are too thin and permeable to mask the wet etching between the deposited gold layer and the silicon wafer in the used etching solution. In order to remove the gold layer and the microgels after MACE, the substrates were exposed to I_2/KI (Sigma Aldrich, 99 %) solution (1:4:40, I_2/KI/H_2O) and O_2 plasma for 30 min. The VA-SiNWs were dried in a CO_2 supercritical drier (Autosamdri-931, Tousimis). Both, the VA-SiNWs and gold core honeycomb structures were characterized with a LEO 1530 SEM (Zeiss, 5 kV) with the in-lens detector, taking 30° tilted images for the VA-SiNWs to measure their height. In order to obtain an additional degree of freedom in the NWs fabrication, a new technique was developed by dipping the substrate to etch in a controlled way with a linear motion driver. This way it was possible to subject different areas of the substrate to different etching times producing continuous gradients on the NW height which here we call "vertical" gradients. In particular, the substrate in Fig. 3c was immersed in the dipping etching solution with an increasing speed profile: 4 min at $25\,\mu m/s$, 2 min at $50\,\mu m/s$, 1 min at $75\,\mu m/s$ and 30 s at $100\,\mu m/s$. The total time of etching was 8 min.

Numerical simulations data

The reflectance was simulated using three-dimensional finite difference time domain simulation (Lumerical FDTD) with periodic boundary conditions in the plane that spanned the NWs, taking into account a single unit cell. Incident plane waves were used as light source and multiple reflections were avoided by perfectly matching layers. Silicon properties were taken from the software materials library (Palik). For the simulations, we chose the experimental values extracted from the substrate in Fig. 3a: diameter of big NWs: 533±23 nm, diameter of small NWs: 130±14 nm, interspacing between big NWs: 1.39±0.12 μm, interspacing between small NWs: 465±52 nm, interspacing between big and small NWs: 737±77 nm.

Optical measurements

For the normal-reflectance in bright field, the samples were measured with a JASCO MSV-370 micro-spectrophotometer in reflection mode, using an aperture of $100x100\,\mu m^2$ and normalizing to the reflectance of a silicon blank substrate. In the case of

the longer NWs which give a lower signal level, we applied a low-pass smoothing to the curves to remove part of the high frequency noise. For the dark-field reflectance measurements, the samples were illuminated by a halogen lamp, focused through a 50x dark-field objective (Zeiss Epiplan Neofluar) and the scattered light was then detected with a spectrophotometer (Acton Series 2300, Princeton Instrument and thermoelectrically cooled camera Pixis 256E). The optical fiber of the imaging spectrometer acted as a pinhole and restricted the collection area around the measured nanoparticle to a disk with a diameter of $30\,\mu m$. The reflectance was normalized to the reflectance of a teflon substrate.

Additional results

Table S2 summarizes the particle diameters in bulk and after deposition on a silicon substrate. We characterized the compression isotherm and corresponding depositions on silicon substrates of the big microgels in Fig. S1. The compression of the small microgels is thoroughly described in previous works[6,7]. For the realization of binary systems, first we tried to pre-mix big and small microgels in water in a ratio of 1:6 of big to small microgels, but due to their opposite charge in MilliQ water conditions (Fig. S2a), they aggregated, as it can be seen in Fig. S2b. This aggregation in bulk was avoided using water at pH 9 (adjusted by adding HCl and NaOH at 1 mM to the water), where both particles are negatively charged. Nevertheless, after deposition at the water/hexane interface and subsequently after transfer to the silicon substrate, they were not arranged into uniform binary lattices, but in local domains of each particle size (Fig. S3a). Injecting sequentially first the big microgels and then the small microgels at the interface (Fig. S3b) or simultaneously co-injecting them from two separate syringes (Fig. S3c), also resulted into separated domains of big and small microgels. Decreasing the surface pressure to provide more available space at the interface or annealing the interface compressing and expanding the monolayer at the interface at 0.1 Hz and 5% of area change, did not improve the microstructure of the patterns.

In Fig. S4 we characterized the re-swelling in water of the big microgels deposited on the silicon substrate by in-situ AFM imaging before and after re-swelling in water (Fig. S4a and b). Additionally, fluorescently labeled big microgels where imaged in-situ before and after 30 min of re-swelling in water, confirming that there was no desorption nor rearrangement after re-swelling. Moreover, in Movie S1, we imaged and characterized the limited re-arrangement of the big microgels deposited on the silicon wafer (at Π ~5 mN/m and Π ~10 mN/m) when crossing the water/oil interface for the second time. Thus, we mimic the second deposition but without small microgels at the interface. After this experiment we could consider that the big microgels do not significantly move during the second deposition of small microgels.

In Fig. S5a we show that at the edge of a region covered by big microgels, the surface coverage of the small microgels is higher. This visual observation can be quantified in Fig. S5b by looking at the position of the first peak of g(r) for the "free" microgels as opposed to the ones deposited in between the big ones, where a smaller spacing is found in the former case. Moreover, we show in Fig. S5c, the rare case of of a small microgel deposited on top of a big microgel, due to the steric repulsion between the re-swollen big microgels and the newly deposited small ones.

In Fig. S6a-g, we provide extended information on the FFT, radial distribution function and autocorrelation of the hexagonal Ψ_6 and triangular Ψ_3 order parameters, corresponding to the binary arrays depicted in Fig. 2a, over different positions along the substrate with corresponding color-coded AFM height images. The order parameters are defined as $\Psi_n = \left\langle \frac{1}{N_b} \left| \sum_{j=1}^{N_b} \exp(in\theta_j) \right| \right\rangle$, n determines the order parameter we calculate, N_b is the number of nearest neighbours, θ_j is the angle formed between a given particle, the x-axis and the line joining the centers of the particle and the j neighbour. Moreover, we calculate the spatial autocorrelation G_6 and G_3, of the Ψ_6 and Ψ_3 parameters, respectively, as $G_n(\chi) = \langle \Psi_n(x)\Psi_n^*(x+\chi) \rangle$, where Ψ_n^* is the conjugate of Ψ_n, and χ is the radial distance at which the autocorrelation function is evaluated.

In Fig. S7a-c, we provided evidence of the possibility to compress continuously the big microgels during the first deposition between 2 to 10 mN/m, keeping this time the small microgels at fixed 5 mN/m during the second deposition. We provide the corresponding FFT and radial distribution function of big and small microgels separately.

In Fig. S8a, we report the particle diameter of big and small microgels after deposition as a function of O_2 plasma etching time. Furthermore, in Fig. S7b we explored the effect of 20 s of O_2 plasma etching before the second deposition, with the same surface pressures as in Fig. 2a. In this way, we could state that at low Π_{small} (i.e. 2 mN/m) the crystalline structure is better after an

Table S2. Microgel diameters in bulk D_{bulk}, measured in MilliQ water (~pH 5.5) by DLS, and after deposition from the water/hexane interface D_i, from AFM measurements (see AFM imaging and particle tracking analysis section) after deposition on a silicon substrate, and composition.

	D_{bulk} (nm)	D_i (nm)	Composition
big[3]	940 ± 10	1630 ± 80	PNIPAM-co-N-(3-aminopropyl)methacrylamide hydrochloride
small[7]	213 ± 10	546 ± 50	PNIPAM-co-methacrylic acid
gold-core[2]	340 ± 17	480 ± 26	(75 ± 2) nm gold core + PNIPAM

intermediate plasma step, as it is the case in the right picture in Fig. 1c, but there is aggregation with the big microgels at higher surface pressures (i.e. above 10 mN/m).

The swelling with photoresist of the big microgels is reported in Fig. S9 and in[5] for the small microgels.

Fig. S10a shows a sample after photoresist swelling and sputtering of 10 nm-thick gold layer, before carrying out the MACE for the sample corresponding to Fig. 3a. Fig. S10b depicts a side view of the NWs with similar deposition parameters as in Fig. S10a, etched for 6 min. Fig. S10c depicts a big area of the same substrate as Fig. 3a to show that the process is robust. The two insets show the capillary aggregation of the NWs when CO_2 supercritical drying is not used after the wet etching and the possibility to harvest the NWs for further applications. Extended information on the substrate depicted in Fig. 3c is shown in Fig. S11, where the additional degree of freedom for the vertical etching is demonstrated obtaining a continuous gradient in length of the NWs. This gradient is perpendicular to the gradient of interparticle distance, for a binary array where the big microgels were deposited at fixed 2 mN/m and the small microgels were compressed from 1 to 19 mN/m. Details of the setup are provided in this picture. As aforementioned, the sample was immersed with an increasing speed profile: 4 min at $25\,\mu m/s$, 2 min at $50\,\mu m/s$, 1 min at $75\,\mu m/s$ and 30 s at $100\,\mu m/s$. Thus, the total time of etching was 8 min, corresponding to the MACE time for the first part of the substrate that was immersed in the etching solution, while the other end was exposed for up to 10 s. Extended information on the simulations reported in Fig. 4 is given in Fig. S12, and dark-field reflectance experimental measurements and simulations in Fig. S13, where we expose the broadening and shifting of peaks of experimental curves in comparison to simulations.

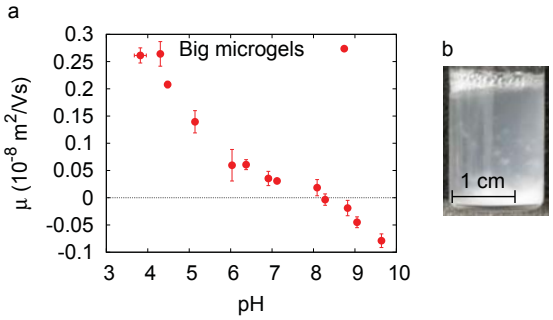

Fig. S2. (a) pH titration curve for the big microgels, where the electrophoretic mobility is plotted against the pH. The small microgels were negatively charged at all pHs between 3 and 9, from $(-0.05\pm0.02)\cdot10^{-8}\mathrm{m^2V^{-1}s^{-1}}$ to $(-0.22\pm0.02)\cdot10^{-8}\mathrm{m^2V^{-1}s^{-1}}$, respectively. **(b)** Bulk aggregation of big and small microgels when mixed in MilliQ water.

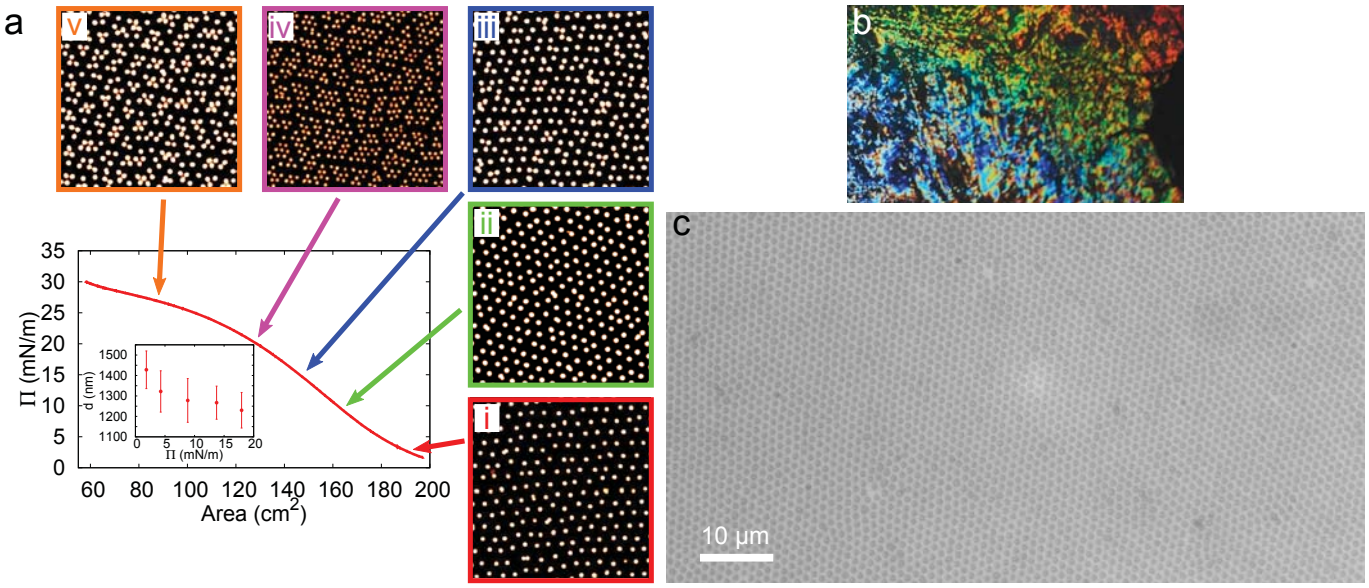

Fig. S1. (a) Compression isotherm of the big microgels at the water/hexane interface and corresponding AFM height images ($20x20\,\mu m^2$), after deposition on a silicon substrate. For the purposes of this work we are interested in the region between 1 to 10 mN/m, corresponding to AFM images (i) and (ii), where microgels show shell-shell contact, and before core-core contact is reached upon compression of the monolayer (iv) and (v). The inset shows the decrease in the interparticle distance d between nearest neighbors upon compression of the monolayer. **(b)** Picture of a $1x2\,cm^2$ silicon substrate with big microgels (deposited at 2 mN/m) deposited over the whole substrate showing opal-like diffraction. **(c)** Optical microscopy image of the substrate in (b).

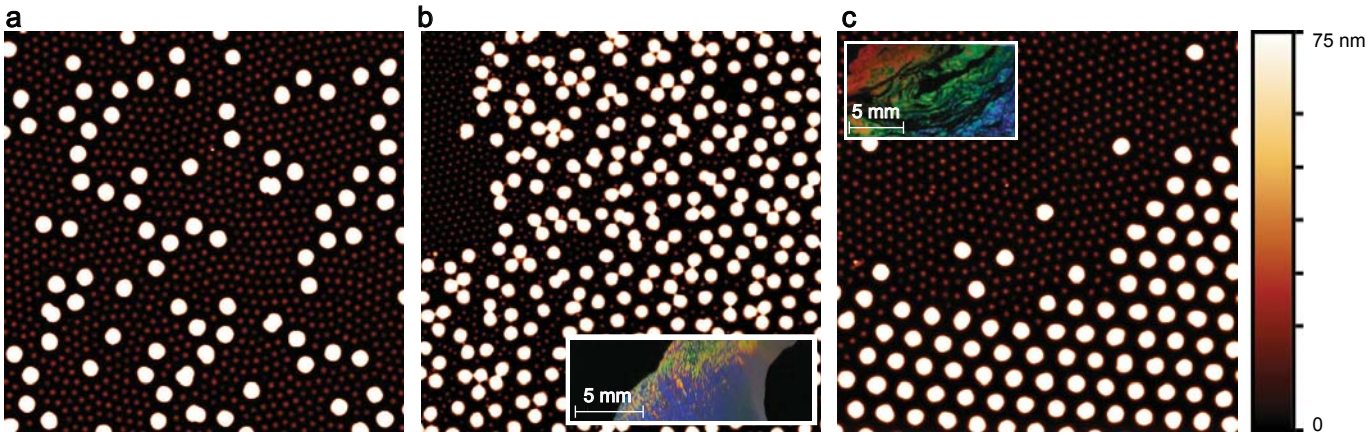

Fig. S3. AFM height images ($20x20\,\mu m^2$) of microgels deposited on silicon substrates depicting binary assembly of microgels in bulk and at the water/hexane interface. **(a)** Microgels pre-mixed in bulk at pH 9 and deposited at the water/hexane interface (also at pH 9). **(b)** A microsyringe was used to inject big microgels first and small microgels in a subsequent step, at the water/hexane interface, working in MilliQ water conditions (~pH 5.5). The inset shows a picture of the substrate exhibiting opal-like diffraction and black domains where the big microgels and small microgels are deposited, respectively. **(c)** Co-injection of both microgels at the interface from separate microsyringes at the same time at the water/hexane interface (in MilliQ water conditions, i.e. pH ~5.5). Again, the inset exhibits opal-like and black domains. The swirls come from shear at the interface during injection, which is not sufficient to mix uniformly the two particle populations.

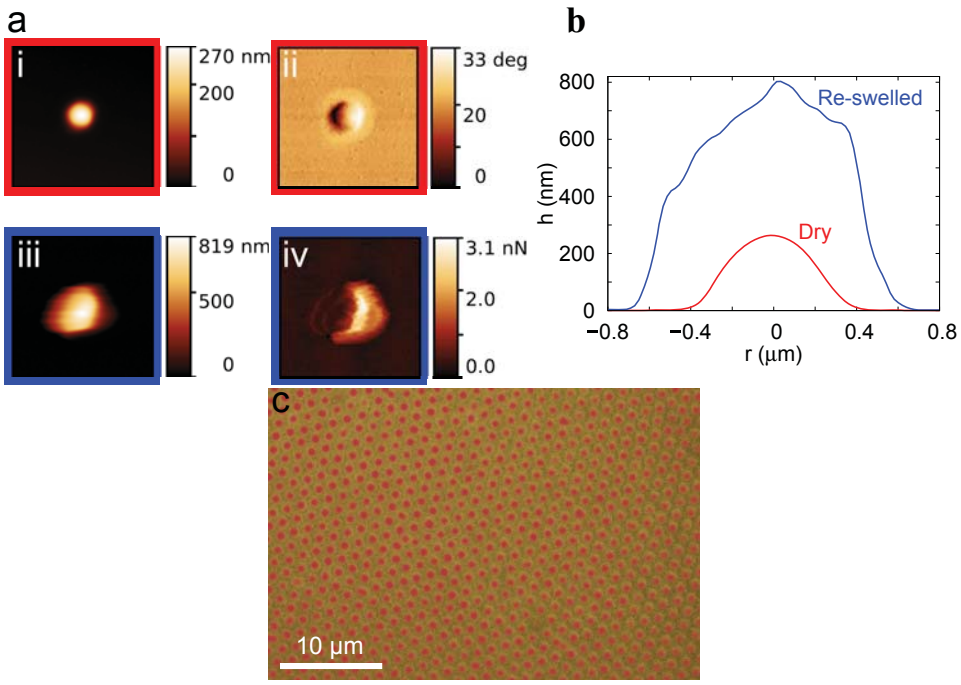

Fig. S4. Characterization of the re-swelling in water for big microgels deposited on a silicon wafer to test their behavior when they are immersed in water for the second deposition of the small microgels. **(a)** AFM images ($3x3\,\mu m^2$). (i) Height and (ii) phase image of a dry big microgel after deposition on a silicon wafer. (iii) Height and (iv) adhesion image of a re-swelled big microgel as the substrate was immersed in water. **(b)** Profiles of the microgel in (a). **(c)** Fluorescent microscopy image of 488 nm-Alexa dye-labeled big microgels deposited on a glass slide before soaking in water (yellow) and after 30 min of soaking in water (over imposed red color). The fluorescent dye was attached via the free amine groups of the big microgels.

Movie S1. Optical microscopy images ($86x46\,\mu m^2$) of a silicon substrate with big microgels, before and after a second "blank" deposition (i.e. passing through the water/hexane interface without deposition of microgels in the second step). It can be seen that only a very limited rearrangement of the big microgels occurs at low $\Pi \sim 5$ mN/m and high $\Pi \sim 10$ mN/m.

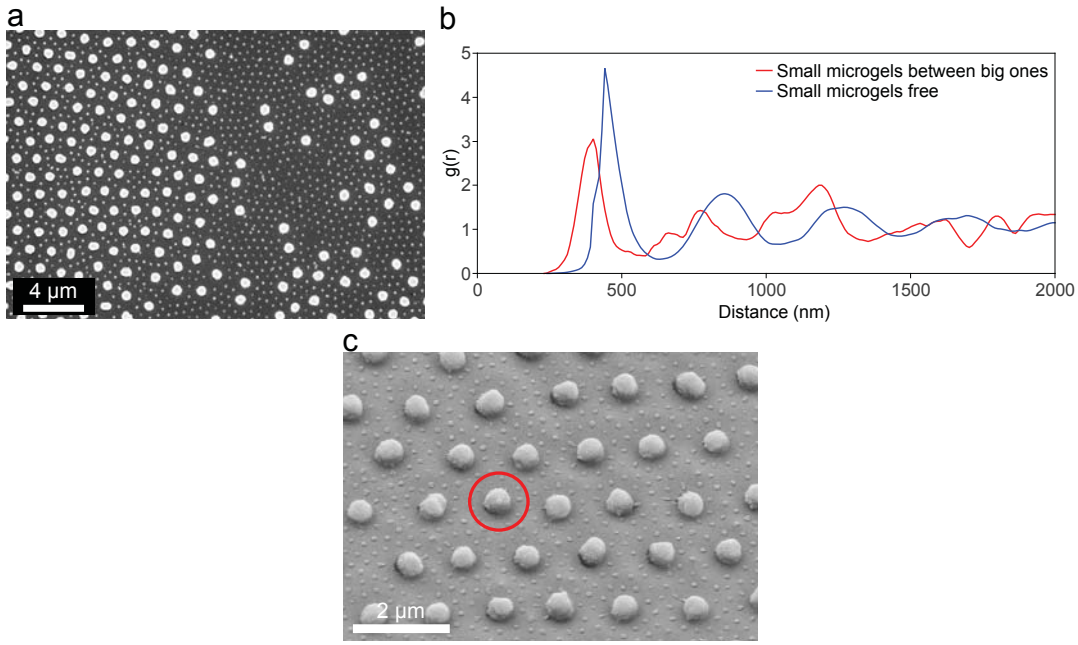

Fig. S5. (a) SEM image of a binary array with a region with no big microgels where small microgels can be seen. **(**b) g(r) of the small microgels of the two areas visible in (a), the red curve corresponding to small microgels deposited around big ones and the blue curve corresponding to "free" microgels. It can be seen that the nearest neighbour distance from the first peak is smaller for the microgels deposited around big microgels than when they are "free". **(c)** SEM image of a binary array where the rare case of a small microgel deposited on top of a big one is shown (red circle).

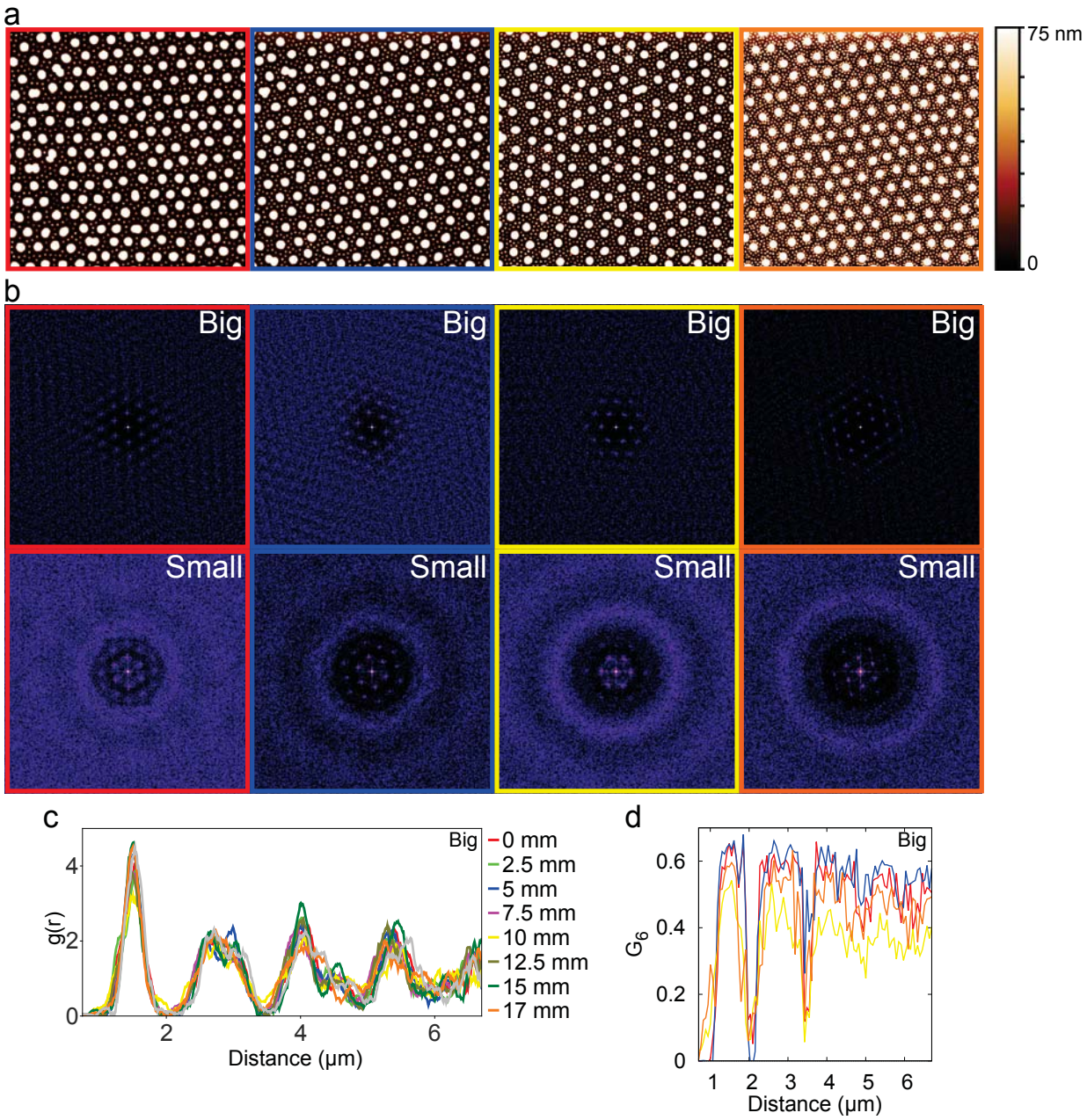
a
75 nm
0
b
Big
Big
Big
Big
Small
Small
Small
Small
c
Big
0 mm
2.5 mm
5 mm
7.5 mm
10 mm
12.5 mm
15 mm
17 mm
g(r)
Distance (μm)
d
Big
G_6
Distance (μm)

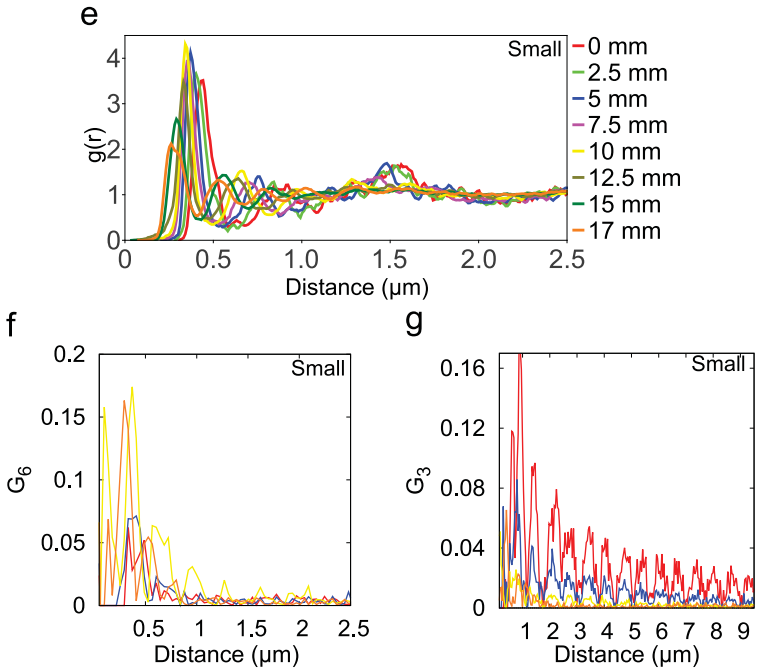

Fig. S6. AFM height images ($20x20\,\mu m^2$) showing adsorption and binary self-assembly of big and small microgels corresponding to the substrate in Fig. 2a-c. **(**b) FFT of the positions of the big and small microgels in (a). **(**c) Radial distribution functions of the big microgels in (a), over different positions along the 2 cm^2 substrate. **(d)** Autocorrelation of the Ψ_6 order parameter for the big microgels in (a). **(**e) Radial distribution functions of the corresponding small microgels in (a). **(f)** Autocorrelation of the Ψ_6 and **(g)** Ψ_3 order parameter for the small microgels in (a). The color code of the images and curves correspond to the positions along the sample given in the legend of panel (e).

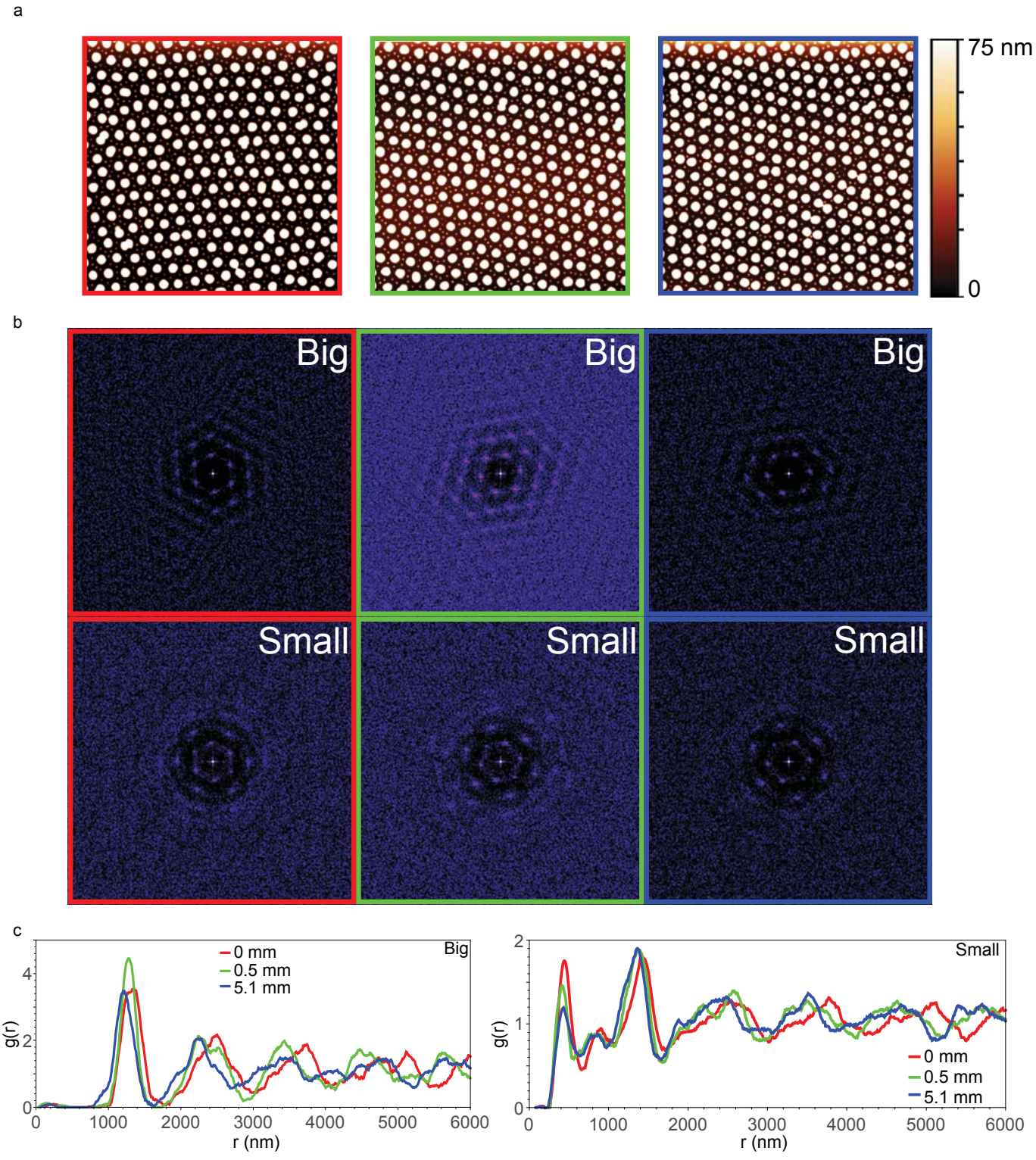

Fig. S7. (a) AFM height images ($20x20\,\mu m^2$) showing the microstructure of a binary microgel array deposited on a silicon substrate of a decoupled continuous gradient where the big microgels were compressed from 2 to 10 mN/m and the small microgels were deposited at a constant surface pressure of 5 mN/m. **(b)** FFT images of the positions of the big and small microgels in (a). **(c)** Radial distribution functions of the big (left) and small (right) microgels corresponding to the AFM images in (a). The color code of the images and curves correspond to the positions along the sample given in the legend of panel (c).

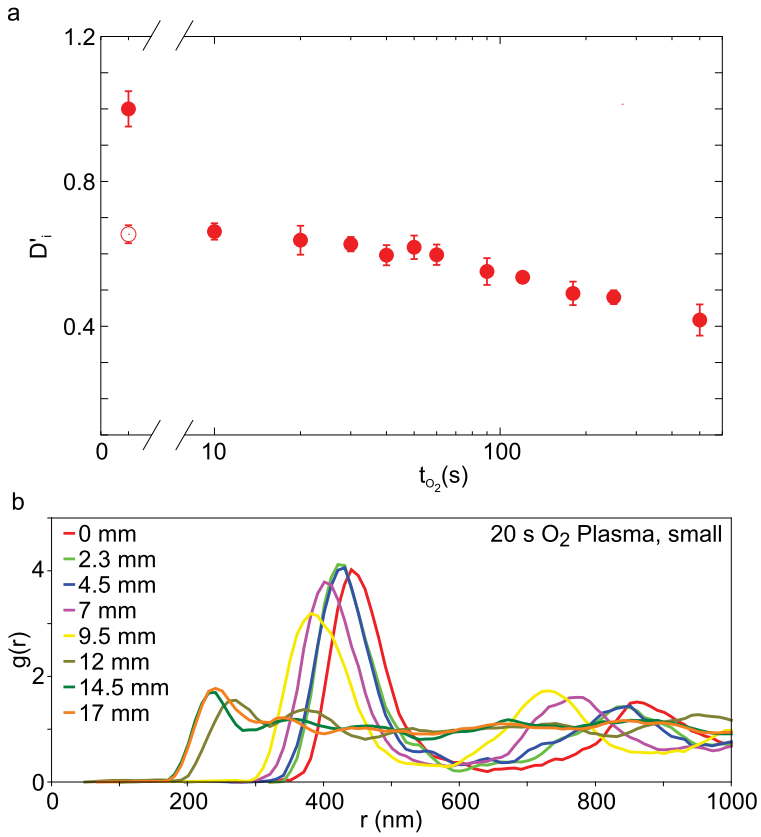

Fig. S8. **(a)** Particle diameter after deposition for big (•) microgels as a function of O_2 plasma etching time. The diameter, D_i', is normalized to its value before plasma, $(1533 \pm 68)\,\mu m$. The same normalization is applied to the diameter of the big particles without the shell after deposition(o). The corresponding data for the small microgels is reported in a previous work[5]. **(b)** Radial distribution function of the small microgels corresponding to the same conditions as in Fig. 2 and S5, but with the big microgels subjected to 20 s of O_2 plasma before the second deposition. Please note the steep change in the position of the first peak at higher surface pressures due to aggregation with the big microgels, which might be caused by the absence of a large swollen corona around the big microgels after re-swelling them in water following the O_2 plasma treatment.

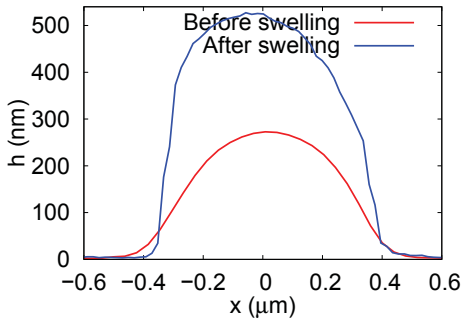

Fig. S9. Profile obtained from AFM height images of the big microgels before and after swelling with the photoresist. The corresponding profiles for small microgels are reported in a previous work[5].

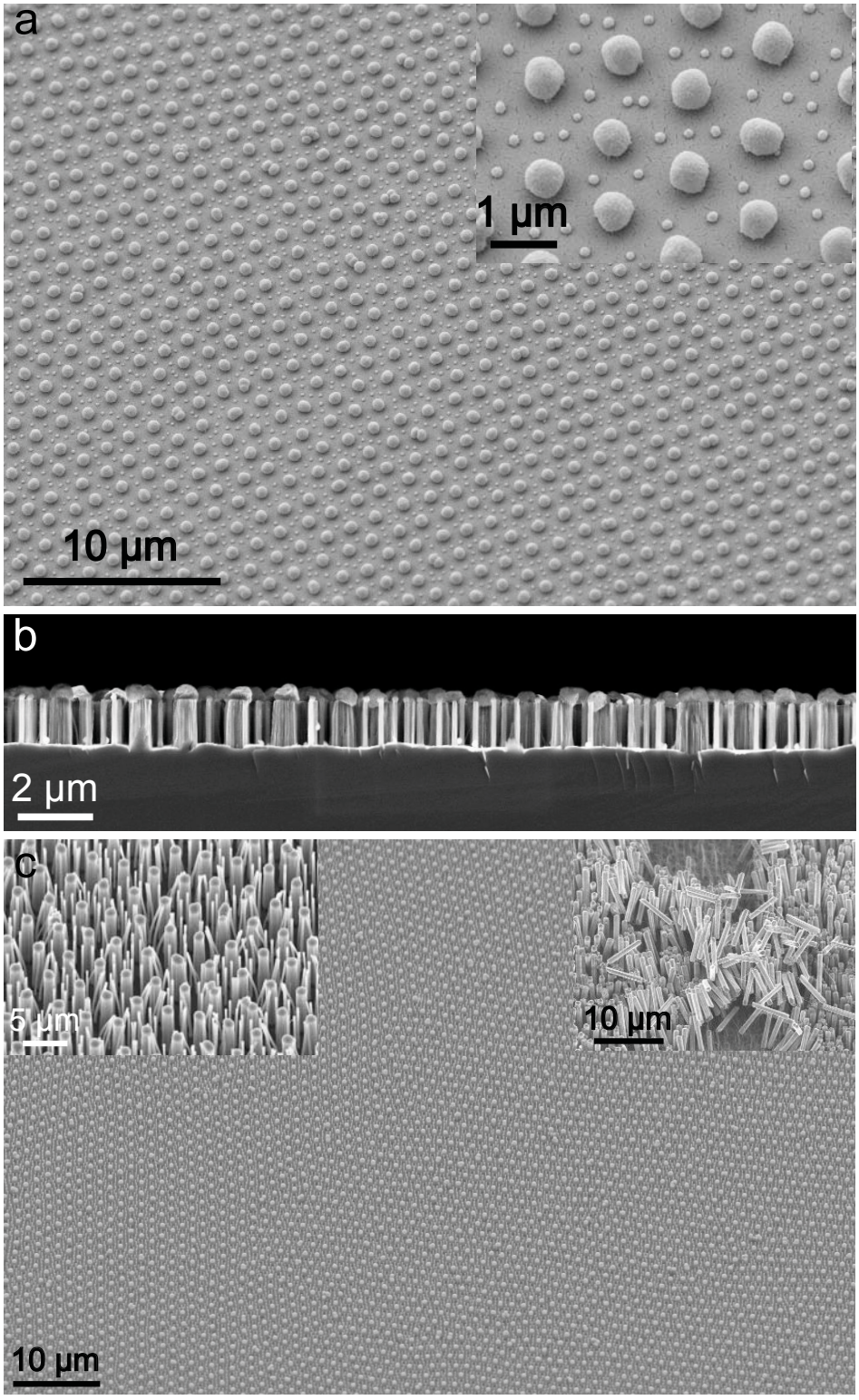

Fig. S10. SEM pictures of **(a)** microgel binary array after swelling with photoresist, followed by sputter coating with 10 nm of gold to produce masks for MACE. The inset is a zoom-in, both images are taken at a tilt angle of 30°. **(b)** Binary array after etching for 6 min in the etching solution described above. The image is taken at a tilt angle of 90°, after fracturing the sample. **(c)** Large-scale view of the same substrate as in Fig. 3a, showing the uniformity of the etching process. The left inset shows the bending of the nanowires during drying if they are directly dried from ethanol after the wet etching, without using CO_2 super-critical drying. The right inset shows mechanically broken nanowires, showing that they might be further harvested.

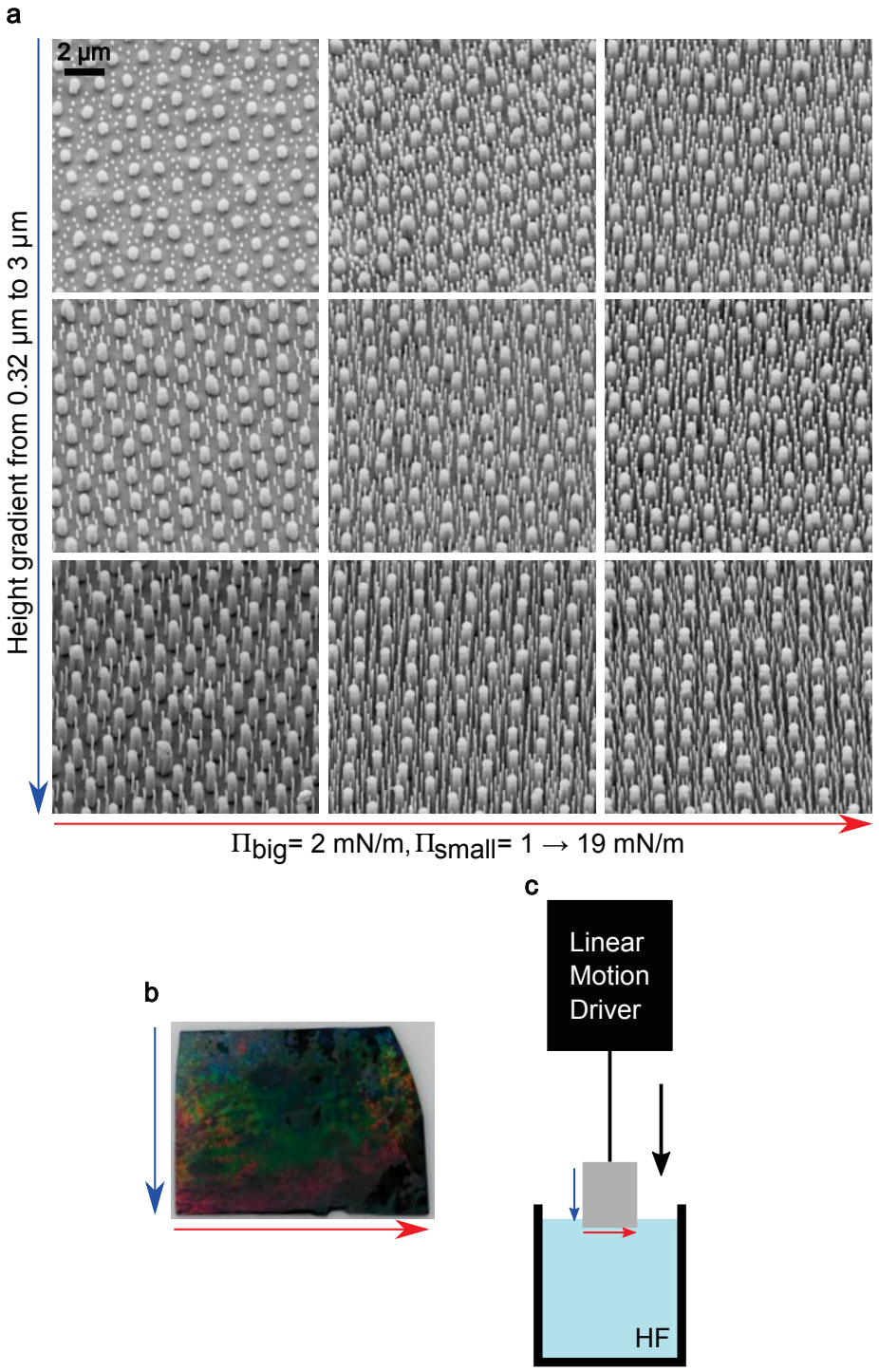

Fig. S11. Characterization of programmable and binary VA-SiNW arrays with continuous gradients in both height and spacing. **(a)** SEM micrographs, corresponding to the design and fabrication of programmable and binary VA-SiNW arrays in Fig. 3c. Nine different spots were imaged, all images were taken on single substrate. The red arrow indicates that big microgels were deposited on the silicon substrate at a constant surface pressure value of 2 mN/n, while the small microgels were deposited on a gradient of surface pressure ranging from 1-19 mN/m. The blue arrow corresponds to the realization of a continuous gradient in height (vertical etching). The sample was wet-etched being dipped in the direction perpendicular to the compression gradient using increasing motor speeds from 25 $\mu m/s$ to 100 $\mu m/s$. **(b)** Photograph of the $1.5x2\,cm$ silicon substrate in (a). **(c)** Scheme of the vertical gradient wet-etching.

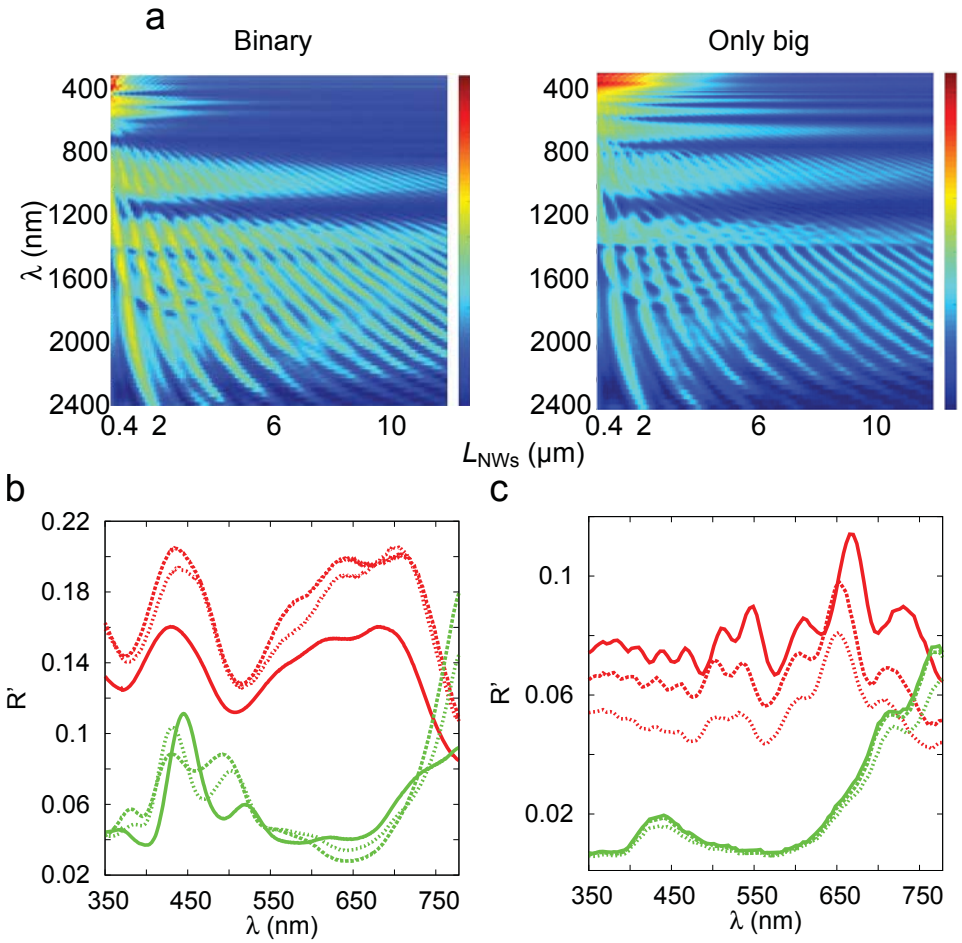

Fig. S12. (a) Extended simulations of the normal reflectance shown in Fig. 4, for different wavelengths λ and VA-NW heights L_{NWs}. Normal reflectance experimental curves obtained for the substrates in Fig. 4 for **(b)** 810 nm-long NWs and **(c)** 3.5 and 3.2 μm-long NWs (red for only big and green for binary arrays, respectively). Curves of the same color and different dashing correspond to measurements in different places over the same substrate.

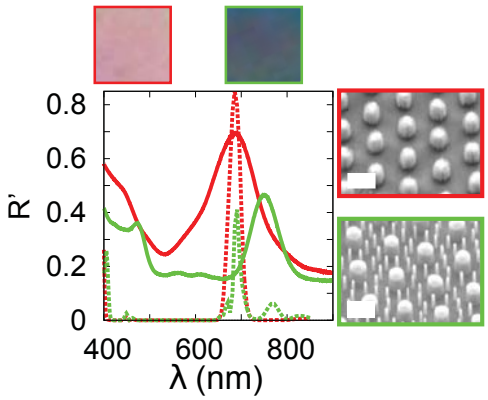

Fig. S13. Experimental (solid lines) and simulation (dashed lines) of the dark-field reflectance taken at 35°for 810nm long binary (green) and "big only" (red) nanowires. The squares on top are 400x400μm digital photographs of the substrates, with structures corresponding to the SEM images on the right (1μm-scale bars). These dark-field spectra originate from a grating effect, where a particular diffracted peak is found at a wavelength $\lambda = \frac{\sqrt{3}}{2}\Lambda \sin\theta/2$, where θ is 35°in our experiments and Λ is the spacing between the big NWs. The presence of the smaller NWs reduces the grating effect, leading to lower reflectivity, but does not change the peak position, as seen in the simulations. The experimental spectra present both broader spectral features and a shift in the peak position, due to NW size polydispersity. In particular, the blue shift in the experiments with the binary NW arrays is compatible with a 10% change in Λ, which is within the measured experimental variations of interparticle spacing.

Patterns with differently sized microgels

In order to show that this process can be used with differently sized microgels, we synthesized big microgels of (582±13) nm (i.e. smaller than the ones reported up to now) and deposited sequentially first the big microgels at a fixed surface pressure of 4 mN/m and then the small microgels in a gradient from 2 to 22 mN/m (Fig. S14).

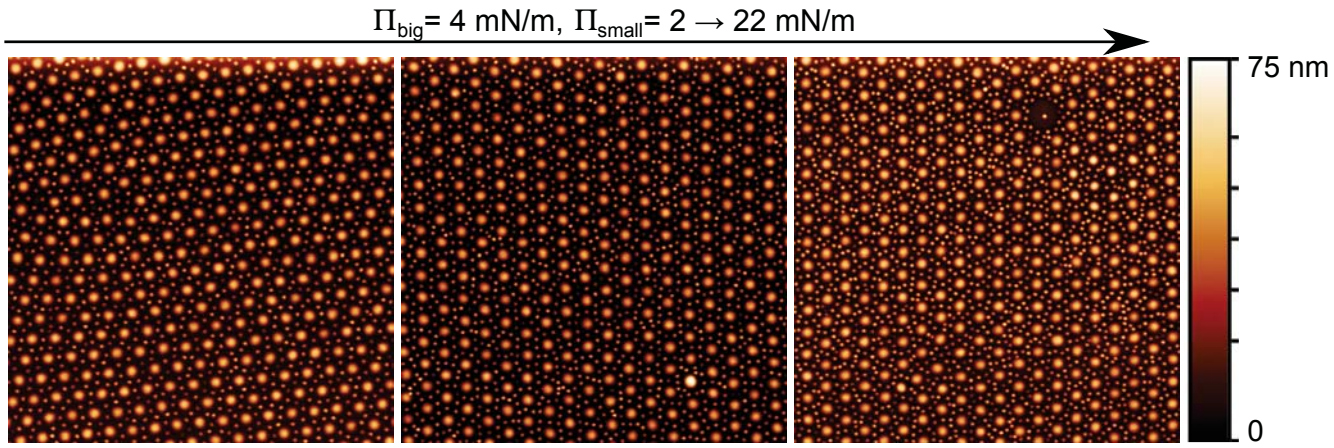

Fig. S14. AFM height images ($20x20\,\mu m^2$) of binary arrays deposited on silicon substrates, produced with big microgels of smaller size, (582±13) nm, at a constant surface pressure of 4 mN/m and a gradient in surface pressure for the small microgels in the range of 2 to 22 mN/m. Please note the big defect in the right image, which it is compensated in the rest of the array thanks to the softness of the microgels.

References

1 K. Geisel, L. Isa and W. Richtering, *Langmuir*, 2012, **28**, 15770–15776.

2 T. Honold, K. Volk, M. Retsch and M. Karg, *Colloids Surf. A*, 2016, **510**, 198–204.

3 G. Conley, P. Aebischer, S. Nöjd, P. Schurtenberger and F. Scheffold, *Sci. Adv.*, 2017, **3**, e1700969.

4 J. Crocker and D. Grier, *J. Colloid Interface Sci.*, 1996, **179**, 298–310.

5 M. Rey, R. Elnathan, R. Ditcovski, K. Geisel, M. Zanini, M. A. Fernandez-Rodriguez, V. V. Naik, A. Frutiger, W. Richtering, T. Ellenbogen, N. H. Voelcker and L. Isa, *Nano Lett.*, 2016, **16**, 157–163.

6 L. Scheidegger, M. A. Fernandez-Rodriguez, K. Geisel, M. Zanini, R. Elnathan, W. Richtering and L. Isa, *Phys. Chem. Chem. Phys.*, 2017, **19**, 8671–8680.

7 M. Rey, M. A. Fernandez-Rodriguez, M. Steinacher, L. Scheidegger, K. Geisel, W. Richtering, T. M. Squires and L. Isa, *Soft Matter*, 2016, **12**, 3545–3557.